Chapter

Single Crystal Hybrid Perovskite Optoelectronics: Progress and Perspectives

Feng Li

Abstract

Organic–inorganic hybrid perovskites, which combine the superior optical and electronic properties and solution-processed manufacturing, have emerged as a new class of revolutionary optoelectronic devices with the potential for various practical applications. Encouraged by the advantages of longer carrier diffusion length, higher carrier mobility and lower trap densities as compared to the polycrystalline counterparts', increasing research attention has focused on preparation and optimization of perovskite crystal candidates, via using various facile growth techniques, for the development of a wide range of optoelectronic applications. This chapter presents a comprehensive review of recent advances in the field of optoelectronic technologies based on different forms of single crystals, including bulk crystals and thin ones, with emphasis placed on the optimization of crystals and the relationship among the charge-carrier transport, operation mechanism, device architecture, and device performance. First, we introduce the main methods used to prepare bulk and thin single crystals, and analyze several aspects of their properties. Thereafter, the applications of single crystals into solar cells, photodetectors, light-emitting diodes, and lasers, are discussed in depth. Finally, we summarize the challenges of perovskite single crystals and propose further improvements in the synthesis approaches and device applications.

Keywords: hybrid perovskite crystals, optoelectronics, solar cells, photodetectors, LEDs

1. Introduction

Perovskite-structured materials have received increasing attention, since being discovered in the 1830s, because of their rich physical properties [1]. As shown in **Figure 1a** [2], the general chemical formula for such compounds is ABX_3, in which A and B are different cations, and X is an anion that bonds to both the A and B cations. Owing to the flexibility of bond angles inherent in the perovskite structure, there are many different distortions that can occur from the ideal structure. Importantly, A can be organic cations, like methylammonium (MA^+) or formamidinium (FA^+) [4–8], B can be metal ions, such as Pb^{2+} and Sn^{2+} [9–12], and X is usually halide ions [13], and such a class of materials is known

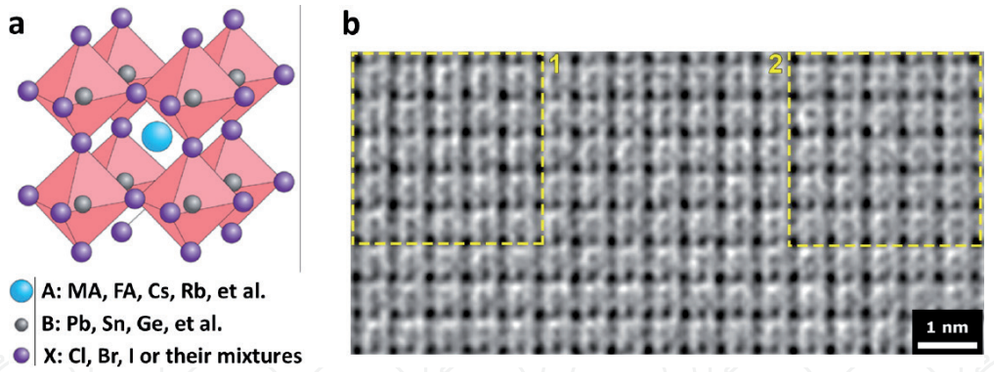

Figure 1.
***1a**, perovskite crystal structure.* Nature Photonics *[2], copyright 2014. **2b**, CTF-corrected high-revolution TEM image.* Science *[3], copyright 2018.*

as organic–inorganic hybrid perovskites. It was reported that a stable structure of hybrid perovskites can form where 0.81 < *T.F.* (tolerance factor) < 1.1 and 0.44 < *O.F.* (octahedral factor) < 0.90 [14]. X-ray diffraction (XRD) measurements were widely used to characterize their structures. As for $MAPbBr_3$ and $MAPbI_3$ crystals, XRD measurements displayed the excellent single crystal properties [15]. Transmission electron microscopy (TEM) measurements were performed to provide a more intuitive picture of perovskite crystals structures (**Figure 1b**), via using contrast-transfer-function corrected method to overcome their electron beam-sensitive property [3]. After the first attempt to employ hybrid perovskite films as active sensitizers into photovoltaic devices [16], hybrid perovskite solar cells have continued to set new efficiency benchmarks [17–23], due to the excellent properties, such as ease of processing, tunable optical band gaps [24, 25], long carrier diffusion length [26], and low trap density [15], as well as large absorption coefficients and high photoluminescence (PL) efficiency [27, 28], and their relatively high power conversion efficiency (PCE) has been increased to as high as 25.2% [29]. Moreover, Leveraging their promising features, hybrid perovskites also have the potential for employment in other optoelectronic applications, including photodetectors [30], transistors [31], phototransistors [32], light-emitting diodes (LEDs) [33], and lasers [34].

However, a vast array of prior research on perovskite optoelectronic devices has been centered on polycrystalline films. The polycrystalline samples usually suffer from grain boundaries, relatively higher trap densities and defects, and low stability, which would obviously obscure their potential in applications [35–37]. More recently, researchers have paid more attention to perovskite single crystals, which possess promising characteristics of no grain boundaries [15], relatively low trap density [38], large charge carrier mobility, and long carrier diffusion length [39–41]. In this regard, extensive efforts are being devoted to developing effective methods to improve the perovskite crystal quality and optimize the device performance. Existing in the forms of bulk or thin crystals, perovskite crystal samples have been widely applied in various optoelectronic applications [39, 42], and have made rapid and great strides in research progress [43–46].

In this chapter, we aim to summarize the recent achievements, ongoing progress, and the challenges to date in the area of hybrid perovskite single crystals, practically MA-based ones ($MAPbX_3$, X = Cl, Br, and I), from the perspective of both materials and devices with an emphasis placed on the optimization of crystal quality, and provide an outlook on the opportunities offered by this emerging family of materials in field of optoelectronic applications.

2. Growth of hybrid perovskite single crystals

2.1 Bulk single crystals

2.1.1 Solution temperature-lowering (STL) method

According to the lower solubility of $MAPbX_3$ in HX (X = Cl, Br, and I) solution as the temperature decreases, Tao's group introduced the STL method to synthesize a $MAPbI_3$ bulk single crystal (**Figure 2a**) [47]. After the reaction between methylamine (CH_3NH_2) and hydro-iodic acid (HI) in a cold atmosphere, the obtained white microcrystal MAI was reacted with $Pb(CH_3COOH)_2{\bullet}3H_2O$ in aqueous HI, and the solution was then cooled to 40°C. A 10 mm × 10 mm × 8 mm black $MAPbI_3$ single crystal was grown in about one month (**Figure 2b**). Lin's group discovered a more efficient way, and they synthesized the single crystals with a size of 5 mm in just around 10 days [48]. Lin et al. selected high-quality seeds and dropped them back into fresh solution and obtained single crystals sized up to 1 cm (**Figure 2c**). Furthermore, $MAPbBr_{3-x}Cl_x$ and $MAPbI_{3-x}Br_x$ mixed-halide perovskite crystals were studied using such method [49]. Hydro-bromic acid with hydrochloric acid or hydro-iodic acid were mixed in different molar ratios into methylamine and lead (II) acetate solution to fabricate single-halide and mixed-halide perovskite crystals (**Figure 2d**). The time-consuming factor is the biggest drawback of this method, which has indirectly led to the domination of other crystallization methods.

2.1.2 Inverse temperature crystallization (ITC) method

As a radically faster perovskite crystal synthesis approach, the ITC method has widely been applied in recent years. It was observed that the exhibited crystals from such method can be shape-controlled, higher quality, and obtained quicker compared with other growth techniques. Bakr et al. introduced this method to rapidly grow high-quality bulk crystals [50]. As shown in **Figure 2e**, an orange $MAPbBr_3$ crystal and a black $MAPbI_3$ crystal were grown within 3 hours. Chen's group further

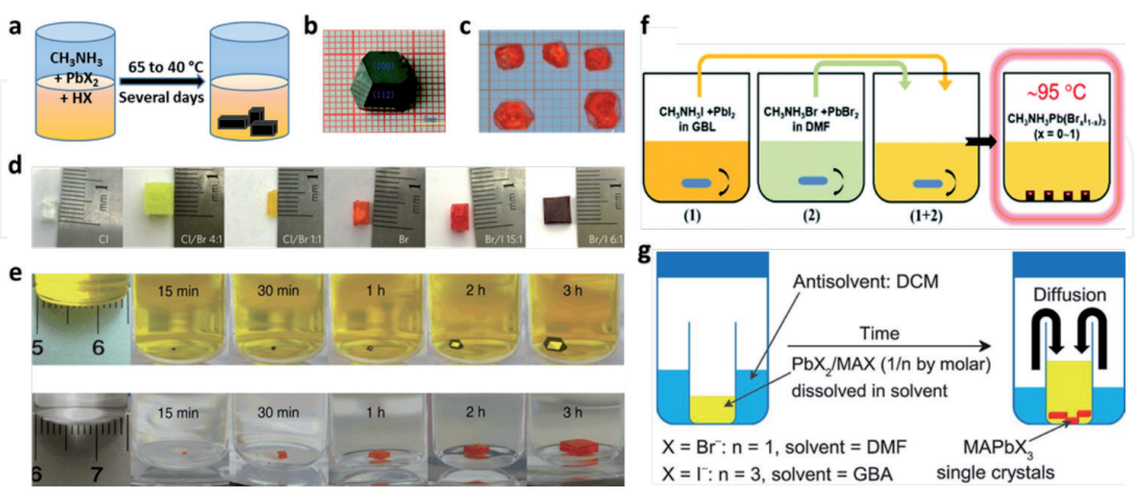

Figure 2.
***2a**, schematic of STL method. **2b**, image of $MAPbI_3$ with {100} and {112} facets.* CrystEngComm *[47], copyright 2015. **2c**, $MAPbBr_3$ crystals from STL method.* J. Cryst. Growth *[48], copyright 2015. **2d**, photographs of perovskite crystals with different halide ratio.* Nature Photonics *[49], copyright 2015. **2e**, $MAPbI_3$ and $MAPbBr_3$ crystals growth at different time intervals.* Nature Commun. *[50], Copyright 2015. **2f**, schematic of crystals growth.* J. Mater. Chem. C *[51], copyright 2016. **2 g**, schematic of AVC method.* Science *[15], copyright 2015.*

studied the effect of molar ratio of MAX and PbX_2 in the precursor solutions on the crystal quality [52], e.g., perovskite crystals with different sizes and shapes were obtained after a 6-hour ITC crystallization process when changing the MAX: PbX_2 ratios from 1:1 to 2:1.

With an aim of growing a large-sized bulk perovskite crystal, such ITC method was further modified. Using such technique, the strategy of incorporation of seed crystal growth has been proven to be favorable for single crystals as large as convenient. Liu's group reported various large-sized perovskite crystals via using the modified ITC method, from which a number of larger-sized crystal (7 mm) were obtained through choosing good-quality seed crystals and repeating and carefully controlling the ITC process several times (**Figure 2f**). Moreover, Liu's group also successfully grew $MAPb(Br_xI_{1-x})_3$ single crystals with a finely-tuned bandgap [51]. The application of the different solubility of different perovskite single crystals at varying temperatures contributes to the time-saving feature of such ITC method.

2.1.3 Anti-solvent vapor-assisted crystallization (AVC) method

Another main method to grow perovskite crystals is the AVC method (**Figure 2g**), which was first introduced from Bakr's group [15]. In this method, the solvent plays a significant role because two or more solvents should be selected, of which one should be a good solvent that is less volatile, and the other is a bad solvent that is more volatile. The principle of this method can be described as follows: when the bad solvent slowly diffuses into the precursor solution, the proficiency of the crystal formation increases at the bottom of the sample vial owing to the insolubility of the material in the bad solvent. Other groups, like Loi's group and Cao's group, also applied this method to obtain the high-quality crystals [38, 53]. Although the AVC method costs more time than the ITC method, its temperature-irrelevant characteristic is appealing to its widespread use.

2.2 Thin single crystals

Bulk perovskite single crystals with thick sizes may cause the increase of charge recombination, which would lead to the degradation of their device performance and impede the practical applications. In this regard, growing thin perovskite crystals with a large area represents an effective approach to overcome the above obstacle and thus advances the further practical applications. Bakr et al. introduced a cavitation-triggered asymmetrical crystallization strategy, in which a very short ultrasonic pulse (≈1 s) was applied in the solution to reach a low supersaturation level with anti-solvent vapor diffusion and a thin crystal with several-micrometers grew on the substrates within hours (**Figure 3a**) [54]. Liu's group synthesized perovskite crystal wafers with a much thinner thickness using a dynamic flow micro-reactor system [55]. They put two thin glass slides in parallel into a container with a predefined separation to grow single crystals within the slit channel, as shown in **Figure 3b**. Su's group further used a space-limited ITC method and grew a 120-cm^2 single crystal on fluorine-doped tin oxide (FTO)-coated glass, of which the operation and the obtained 0.4-mm-thin single crystal are shown in **Figure 3c** [56]. Meanwhile, Wan et al. reported a space-confined solution-processed method to grow the perovskite single-crystalline films with adjustable thickness from nanometers to micrometers (**Figure 3d**) [57]. Benefitting from the capillary pressure, the perovskite precursor solution filled the whole space between two clean flat substrates, which were clipped together and dipped in the solution.

Currently, more promising approaches have been employed to grow thin single crystals with high quality and large scale. A one-step printing geometrically-confined

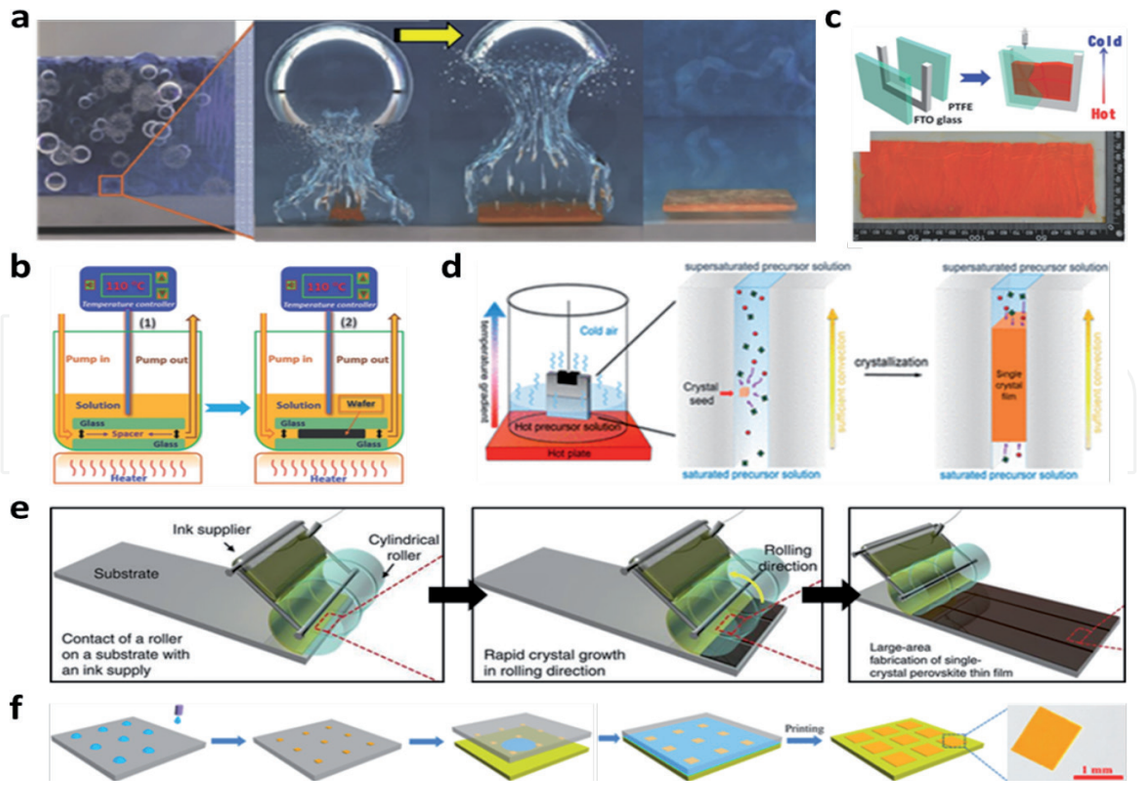

Figure 3.
3a, *schematic of cavitation-triggered asymmetrical method.* Adv. Mater. *[54], Copyright 2016.* ***3b,*** *schematic of ultrathin crystal wafer growth.* Adv. Mater. *[55], Copyright 2016.* ***3c,*** *schematic of the laminar $MAPbBr_3$ crystal films preparation.* Adv. Mater. *[56], Copyright 2017.* ***3d,*** *schematic for the growth of perovskite thin crystals.* J. Am. Chem. Soc. *[57], copyright 2016.* ***3e,*** *schematic of geometrically-confined lateral crystal growth method.* Nature Commun. *[58], Copyright 2017.* ***3f,*** *schematic of the scalable growth for perovskite crystal films using an inkjet printing method.* Sci. Adv. *[59], Copyright 2018.*

lateral crystal growth method (**Figure 3e**) was introduced by Sung's group to obtain a large-scaled single crystal [58]. During the process, a cylindrical metal roller with a flexible poly-(dimethyl-siloxane) (PDMS) mold was wrapped and then rolled on a preheated SiO_2 substrate (180°C) with an ink supplier filled with the precursor solution. Alternatively, millimeter-sized single crystals were synthesized by Song's group by a facile seed-inkjet-printing approach (**Figure 3f**) [59]. Perovskite precursor solution was injected onto a silicon wafer, and then the ordered seeds were formed on the substrate with the evaporation of the droplets. Thereafter, the substrate with a saturated perovskite solution was covered and the single crystals can be grew as the solvent dried at room temperature. Seeds were used to inhibit the random nucleation and trigger the growth of single crystals.

As discussed above, some optimized space-limited approaches have been introduced and developed to synthesize perovskite thin crystals in recent years. Especially, size−/thickness-controlled thin crystals have also been widely used in various optoelectronic devices. With the aim to growing large-scaled and thickness-controlled thin crystals with longer carrier diffusion lengths, fewer defects, and higher efficiency, more promising strategies will be rewarding in the future.

3. Optoelectronic characterizations of perovskite single crystals

3.1 Optical properties

There are two normal ways to study the optical properties of hybrid perovskite crystals: absorption and PL measurements. Bakr et al. characterized the steady-state

absorption and PL properties for $MAPbBr_3$ and $MAPbI_3$ crystals, as shown in **Figure 4a** and **b** [50]. Sharp band edges were observed in the absorption plots and the band gap values were determined to be 2.18 eV for $MAPbBr_3$ crystals and 1.51 eV for $MAPbI_3$ crystals; while the PL intensity peaks are located at 574 nm for $MAPbBr_3$ and 820 nm for $MAPbI_3$. As for the $MAPbCl_3$ one, absorption measurement result revealed an edge at 435 nm (**Figure 4c**) [60]. Clearly, the optical absorption of perovskite crystals exhibited a clear-cut sharp band edge, which indicated that the single crystals are predominantly free from grain boundaries and have relatively low structural defects and trap densities.

More recently, there have been more broad publications on the apparent disparity in optical properties (i.e., absorption and PL) between perovskite single crystals and thin films, which can be attributed to the incorrect measurements as a result of reabsorption effects. Snaith's group performed a detailed investigation of the optical properties of $MAPbBr_3$ crystals as compared to those of the polycrystalline films by employing light transmission spectroscopy, ellipsometry, and spatially resolved and time-resolved PL spectroscopy [61]. They showed that the optical properties of the perovskite crystals were almost identical to those of polycrystalline films, and their observations indicated that the perovskite polycrystalline films were much closer to possessing 'single-crystal-like' optoelectronic properties than previously thought, and also highlighted the discrepancies in the estimation of trap densities from the electronic and optical methods (**Figure 4d**). For the further development of perovskite crystals, more detailed experimental investigations combined with theoretical calculations that focus on the optical features are required, which would assist in the preparation of the high-quality perovskite single crystals and the development of the high-performance device applications.

3.2 Charge transport properties

As for hybrid perovskite crystals, in addition to the remarkable optical properties, their promising electrical properties have caught the great attention. In general, there are five common methods to measure the transport mobilities in perovskite crystals, including the space charge limited current (SCLC), time-of-flight (TOF), Hall Effect, THz pulse and field-effect transistor (FET) measurement methods. Among these methods, the SCLC method is widely employed to determine the carrier mobility and trap density of perovskite crystals. The current–voltage (*I-V*) curve can be divided into three parts: the first region, where an Ohmic contact exists, hence the conductivity can be estimated; the second region is the trap-filling region, which is increased sharply at trap-filled limit voltage (V_{TFL}); and the third region, known as the child region. Trap density (n_{trap}) can be obtained by following the relation: $n_{trap} = (2V_{TFL}\varepsilon\varepsilon_0)/(eL^2)$, where ε_0 is the vacuum permittivity, ε is the relative dielectric constant, L is the crystal thickness, and e is the electron

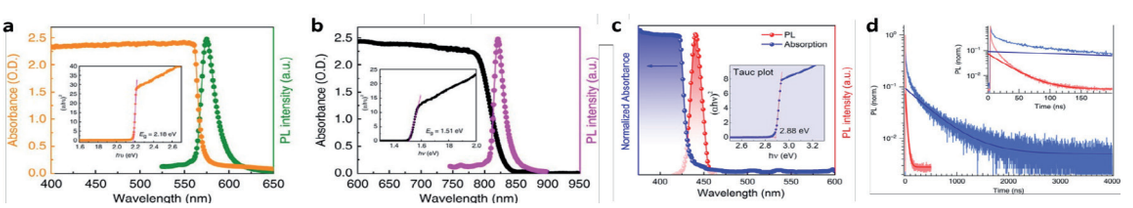

Figure 4.
*Steady-state absorption (**4a**) and PL spectra (**4b**) of $MAPbBr_3$ and $MAPbI_3$ crystals, respectively.* Nature Commun. *[50], Copyright 2015.* **4c**, *steady-state absorption and PL spectra of $MAPbCl_3$ crystal. Insets: Band gap for the above single crystals.* J. Phys. Chem. Lett. *[60], Copyright 2015,* **4d**, *normalized PL decays for $MAPbBr_3$ film (red) and crystal (blue) excited at 447 nm. Inset shows the zoom on the shorter time scale.* Nature Commun. *[61], Copyright 2017.*

charge. Moreover, the mobility (μ) is determined by fitting the *I-V* curve with Mott-Gurney's law: $\mu = (8JL^3)/(9\varepsilon\varepsilon_0 V^2)$, where J is the current density. Liu's group designed the hole-only device (**Figure 5a**), and a large hole mobility of 67.27 cm^2/Vs was estimated [62]. An SCLC method was also applied on $MAPbBr_3$ crystals, with an n_{trap} of 5.8×10^9 cm^{-3} and a μ of 38 cm^2/Vs [15]. *I-V* response of a $MAPbCl_3$ crystal was measured by Bakr's group with $n_{trap} = 3.1 \times 10^{10}$ cm^{-3} and $\mu = 42$ cm^2/Vs [60]. Another method to measure the μ is the TOF method. Bakr's group obtained the μ via using the TOF method (**Figure 5b**) [15], from which μ can be defined by the equation: $\mu = d^2/(V\tau_t)$, where d is the sample thickness, V is the applied voltage, and τ_t is the transit time that be provided by the transient current under different driving voltages [67, 68]. The same method was also applied by Huang's group and the electron μ was verified to be 24.0 ± 6.8 cm^2/Vs (**Figure 5c**) [63]. Apart from the above two methods, Bakr et al. also carried out the complementary Hall Effect measurements on perovskite crystals, confirming the μ ranging from 20 to 60 cm^2/Vs [15]. Meanwhile, Huang's group applies the Hall Effect measurement [68], and they showed the crystals were slightly p-doped with a low free holes concentration. Thereafter, Podzorov's group increased the conductivity of $MAPbBr_3$ single crystals by sputtering Ti on the flat-faceted single crystal to form Hall bars (**Figure 5d**) [64], from which the Hall mobility was calculated to be 10 cm^2/Vs.

Although the above measurement approaches have been widely used in the perovskite crystals, the obtained results from different groups are sometimes different. Sargent et al. demonstrated that one main challenge that may explain these order-of-magnitude discrepancies is that the Hall Effect, TOF, and SCLC methods all probe the mobilities near the respective Fermi levels during the experiments, and the (non-equilibrium, high-injection-level) Fermi level is widely different in each experiment [64]. In this regard, they developed a contactless method to measure the mobility of a perovskite crystal directly [64]. Plus, THz pulse measurement was also used to estimate μ. David et al. used a two-color laser plasma in dry air to generate multi-THz pulses and excited the large $MAPbI_3$ single crystals and detected the electric field by an air-biased coherent detection scheme with 1–30 THz ultrabandwidth after normal incidence reflection off the crystal facet (**Figure 5e**, **f**) [65]. Such spectra measurements indicate the ultrafast dynamics and efficiencies of free charge creation and remarkably high μ as high as 500–800 cm^2/Vs. Furthermore, FETs are the fundamental components to realize digital integrated circuits, which are also often used as a platform to evaluate charge transport mechanism in the active materials. In this regard, bottom-gate, top-contact FETs were fabricated via using micrometer-thin $MAPbX_3$ (X = Cl, Br, and I) crystals as active layer (**Figure 4g**) [66], from which the field-effect μ values are up to 4.7 and 1.5 cm^2/Vs in p- and n-channel devices, respectively (**Figure 5h**).

Carrier lifetime (τ) is an important parameter that should be considered when designing an optoelectronic device. Upon excitation by photons, the active materials will be in an excited state. After that, the photo-induced holes and electrons will recombine back to the ground state. Usually, if this recombination process, that is, the carrier lifetime of carriers, is sufficiently long, a high performance device will be expected. The τ of semiconductors strongly depends on the nature, dimension, and purity of the materials. Generally, τ can be obtained from the PL decay, transient absorption, as well as the transient photo-voltage decay and impedance methods [69]. Among these methods, the PL decay approach has been widely applied. The superposition of fast and slow components of carrier dynamics from the PL spectra measurement result yield $\tau \approx 41$ and 357 ns for $MAPbBr_3$ (**Figure 5i**) [15, 70, 71]. Transient absorption (TA) also suggests the recombination property of excitons which is used to determine the carrier lifetime through a bi-exponential fitting [60]. The carrier diffusion length L_D can be further

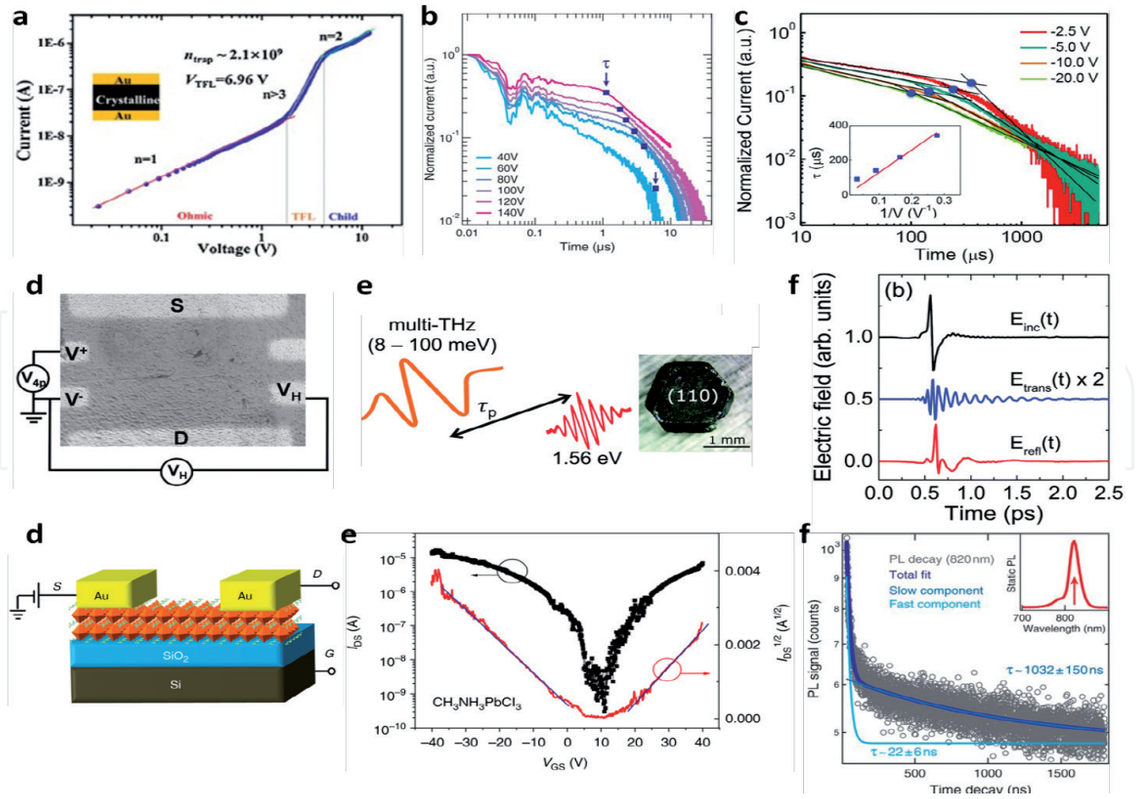

Figure 5.
***5a**, dark* I-V *curve of hole-only $MAPbI_3$ crystal device.* J. Energy Chem. *[62], Copyright 2018.* ***5b**, ToF traces of $MAPbBr_3$ crystal.* Science *[15], copyright 2015.* ***5c**, transient current curves of perovskite crystal devices.* Science *[63], copyright 2015.* ***5d,** schematic of hall effect measurement.* Adv. Mater. *[64], Copyright 2016.* ***5e**, schematic of time-resolved multi-THz spectroscopy experiment.* **5f**, *incident (black), transmitted (blue) and reflected (red) multi-THz pulses after interaction with the crystal.* Energy Environ. Sci. *[65], Copyright 2015.* ***5 g**, schematic of bottom-gate, top-contact perovskite crystal FET.* ***5 h**, transfer characteristics of a $MAPbCl_3$ device.* Nature Commun. *[66], Copyright 2018.* ***5i,** PL time decay trace of a $MAPbBr_3$ crystal.* Science *[15], copyright 2015.*

estimated based on the equation: $L_D = [((k_BT)/e\mu\tau)]^{1/2}$, where k_B is Boltzmann's constant and T is the sample temperature. From the above-examined values of μ and τ, L_D was calculated [63, 64].

4. Applications of perovskite single crystals

4.1 Photovoltaic cells

The widely studied hybrid perovskite solar cells with high performance are usually made from polycrystalline films; however, the current studies have also focused on the developments and optimization of single crystal perovskite solar cells, owing to their significant advantages. Huang et al. fabricated photovoltaic devices based on $MAPbI_3$ bulk crystals by depositing gold (Au) as anodes and gallium (Ga) as cathodes (**Figure 6a**) [63]. A red-shift of 50 nm of the EQE cutoff to 850 nm showed that $MAPbI_3$ crystals increased the upper limit of short-circuit current density (*JSC*) compared with the polycrystalline solar cells from 27.5 mA/cm^2 to 33.0 mA/cm^2. Notably, as compared with the perovskite polycrystalline solar cells, the bulk crystal devices showed much lower efficiency, which was attributed to the fact that photogenerated carriers could not be fully collected in a thick active layer. Much thinner $MAPbBr_3$ monocrystalline films grown on indium tin oxide (ITO)-coated glass were applied into the solar cells, and the devices showed the best cell performance with a fill factor (*FF*) of 0.58, a *JSC* of 7.42 mA/cm^2, an open-circuit voltage (*VOC*) of

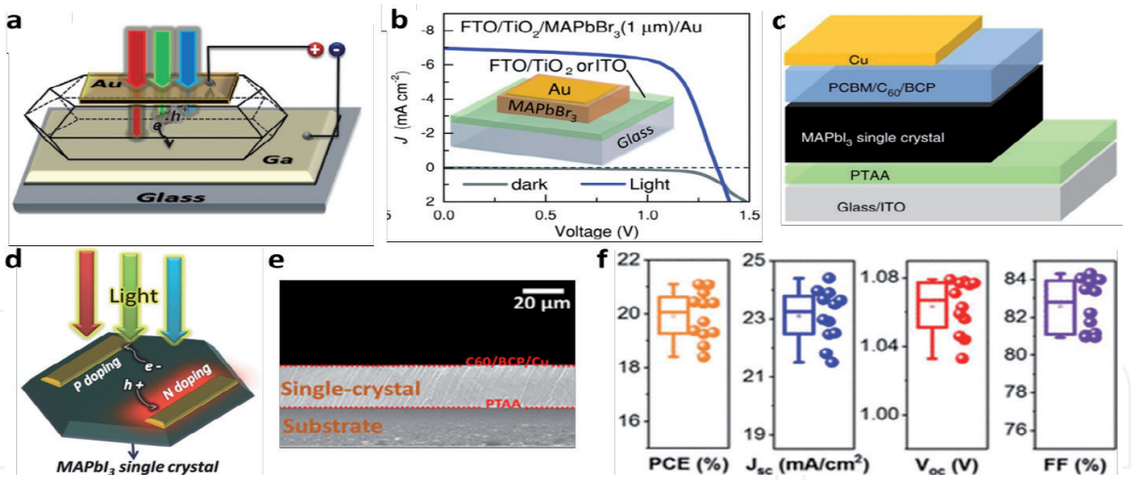

Figure 6.
6a, *schematic of $MAPbI_3$ crystal solar cell.* Science *[63], copyright 2015.* ***6b,*** *dark and illuminated* J-V *curves of $MAPbBr_3$ crystal solar cells with a device illustration in the inset. Adv. Mater. [54], Copyright 2016.* ***6c,*** *device structure of single-crystal solar cells.* Nature Commun. *[72], Copyright 2017.* ***6d,*** *schematic of $MAPbI_3$ crystal solar cells with lateral structure.* Adv. Mater. *[73], Copyright 2016.* ***6e,*** *cross-sectional SEM image of a $MAPbI_3$ crystal device.* ***6f,*** *statistical summary of photovoltaic parameters from 12 devices.* ACS Energy Lett. *[74], Copyright 2019.*

1.24 V, and a *PCE* of 5.37% (**Figure 6b**) [54]. To enhance the device performance, Huang's group further fabricated crystal solar cells through interface engineering (**Figure 6c**), of which the best device showed a *JSC* of 20.5 mA/cm^2, a *VOC* of 1.06 V, a *FF* of 74.1%, and a *PCE* of 16.1% [72]. The single crystal solar cell also displayed the better device stability of remaining nearly unchanged after storage in air for 30 days.

In addition to the vertical-structured solar cells, Huang's group also fabricated the lateral structure perovskite crystal device (**Figure 6d**) [73], which showed a *VOC* of 0.82 V and the highest *PCE* of 5.36% at 170 K. More recently, a 20-μm $MAPbI_3$ single crystal inverted *p-i-n* solar cell with a *PCE* as high as 21.09% and a *FF* up to 84.3% was fabricated [74], of which the cross-sectional SEM image and photovoltaic performance are shown in **Figure 6e** and **f**. To further realize the optimized performance of perovskite crystal solar cells, more efforts will be performed to enhance the sample quality and to design promising device structures.

4.2 Photodetectors

Photodetectors which can convert incident light into electrical signals are critical for various industrial and scientific applications. To evaluate the photodetector performance, several parameters are important, including responsivity (*R*), detectivity (*D**), Gain (*G*), and linear dynamic range (*LDR*), which are listed and are explained in **Table 1** briefly.

4.2.1 In visible region

Huang's group fabricated perovskite crystal photodetectors that exhibited a high sensitivity capacity, which led to a narrow-band photo-response with a full width at half maximum (FWHM) of less than 20 nm under V = −1 V (**Figure 7a**) [49]. *EQE* spectra of the single crystals showed a narrow peak near the absorption edge, which promised a detection application at a specific wavelength, with a peak *D** over 2 × 10^{10} Jones at 570 nm under V = −4 V (**Figure 7b**). Also, Huang et al. further fabricated vertical structured perovskite crystal photodetectors by using the non-wetting hole transport layer-coating substrates [75]. The noise currents are as low as 1.4 and 1.8 fA/Hz$^{1/2}$ at an 8-Hz frequency for the devices based on $MAPbBr_3$

Quantity	Unit	Definition
Photocurrent (I_{light})	A	Current through a photodetector resulting from illumination.
Dark-current (I_{dark})	A	Current through a device in the absence of illumination.
Photoresponsivity (R)	A/W	R is calculated according to: $R = (I_{light} - I_{dark})/P_{light}$, where P_{light} is power of the incident light.
Detectivity (D^*)	Jones	D^* can be calculated as $R/(2eJ_d)^{1/2}$, where e is elementary charge and J_d is dark current density.
Gain (G)	—	G can be calculated as $[(J_{light} - J_{dark})/e]/(P_{light}/h\nu)$, where $h\nu$ is the incident photon energy.
Linear dynamic range (*LDR*)	dB	LDR is calculated by LDR = $20\log(P_{sat}/P_{low})$, where P_{sat} (P_{low}) is the light intensity when the incident light intensity stronger (weaker) than which the photocurrent begins to deviate from linearity.
External quantum efficiency (*EQE*)	%	Carrier number divided by the number of incident photons.
Internal quantum efficiency (*IQE*)	%	It is the ratio of carrier number to the number of incident photons that are absorbed by the device.

Table 1.
Parameters for evaluating the perovskite single crystal photodetectors.

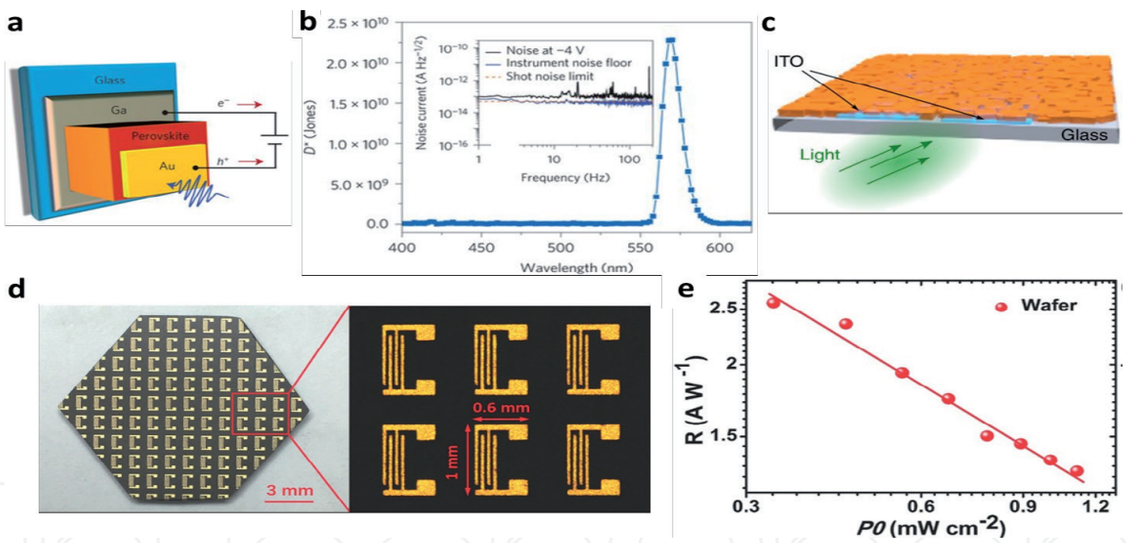

Figure 7.
***7a**, schematic of device structure. **7b**,* D* *spectrum and total noise at −4 V.* Nature Photonics *[49], copyright 2015. **7c**, illustration of planar-integrated $MAPbBr_3$ photodetector.* Nature Commun. *[42], Copyright 2015. Photograph of ≈100 photodetectors on a perovskite crystal wafer (**7d**) and the* R *values (**7e**).* Adv. Mater. *[55], Copyright 2016.*

and $MAPbI_3$, respectively. Additionally, the photocurrent responses of both the $MAPbBr_3$ and $MAPbI_3$ devices were linear, and their *LDR*s are up to 256 and 222 dB, respectively. Sun's group introduced a planar-type photodetector on the $MAPbI_3$ crystal (001) facet with a highest R value of 953 A/W and *EQE* of 2.22×10^5% at a light power density of 2.12 nW/cm^2 [76]. Wei's group used a two-step method to fabricate a self-powered photodetector based on a $MAPbBr_3$ crystal core-shell heterojunction [77]. The device showed a broad photo-response ranging from 350 to 800 nm and a peak R up to 11.5 mA/W. Hu's group fabricated photodetectors based on $MAPbI_3$ single crystal nanowires and nanoplates by transferring them to SiO_2/Si slides [78]. The highest On/Off ratio approached 10^3 under a light illumination of 73.7 mW/cm^2.

Although perovskite crystal photodetectors have shown better performance, macroscopic crystals cannot be grown on a planar substrate, restricting their potential for device integration. To overcome this shortcoming, Bakr et al. grew large-area planar-integrated crystal films onto the ITO-patterned substrates (**Figure 7c**) [42], and the fabricated photodetector possessed a high G (above 10^4) and a high gain-bandwidth product (above 10^8 Hz) relative to other perovskite devices. Furthermore, Liu's group fabricated a photodetector based on a thin perovskite crystal wafer by the space-limited crystallization method, which has about 100 pairs of interdigitated Au wire electrodes (**Figure 7d**) [55], and the R increased linearly as the radiance intensity decreased (**Figure 7e**). Moreover, Su's group sputtered the thin Au electrodes on a large-area $MAPbBr_3$ thin crystal to fabricate a narrowband photodetector [56]. Furthermore, Ma's group reported the superior-performance photodetectors based on $MAPbBr_3$ thin crystals [79], which displayed the R as high as 1.6×10^7 A/W and the highest G up to 5×10^7.

4.2.2 In ultraviolet (UV) region

UV detection is a key technology in the fields of flame detection [80], remote security monitoring [81], environmental monitoring [82], and so forth. Researchers have endeavored to develop UV photodetectors based on perovskite crystals considering their excellent UV absorption properties. Visible-blind UV photodetectors based on $MAPbCl_3$ crystals a suitable bandgap of about 3.11 eV were fabricated (**Figure 8a**) [60], and the device showed the dark current as low as 4.15×10^{-7} A at 15 V and a drastically high stability (**Figure 8b**). Planar-integrated $MAPbCl_3$ crystal UV photodetectors on ITO-deposited glass substrate were reported by Sargent et al. (**Figure 8c**) [83], which showed decreased R and G values as increased power density of a 385-nm laser (**Figure 8d**) [85].

4.2.3 In near-infrared (NIR) region

NIR photodetectors have widespread uses in telecommunications [86], as well as thermal and biological imaging [87–90]. Meredith's group demonstrated the perovskite crystal that overcame the large bandgap and presented photodetectors with performance metrics appropriate for NIR detection by using the trap-related linear sub-gap absorption (**Figure 8e**) [84]. A strong NIR photo-response was achieved in photodiodes based on $MAPbI_3$ crystals illuminated by a continuous 808-nm laser (~10 mW/cm^2). The photodiodes could also respond to a laser with a wavelength as long as 1064 nm (**Figure 8f**).

4.2.4 In X-ray region

In addition to the common light detections from UV to IR, perovskite crystals have been employed for the detection of X-rays, which have important applications in medical diagnostics, clinical treatment, and the non-destructive testing of products [53]. Huang et al. fabricated a sensitive $MAPbBr_3$ crystal X-ray detector with the structure of Au/$MAPbBr_3$/crystal/C_{60}/BCP/Ag or Au (**Figure 9a**) [53]. Through reducing the bulk defects and passivating surface traps, the devices showed a detection efficiency of 16.4% at a near zero bias under irradiation with continuum X-ray energy up to 50 keV. The lowest detectable X-ray dose rate was 0.5 $\mu Gy_{air}/s$ with a sensitivity of 80 $\mu C/Gy_{air}cm^2$, which is four times higher than the sensitivity achieved in α-Se-based X-ray detectors (**Figure 9b**). An X-ray detector based on *p-i-n* diode array made of a thick $MAPbBr_3$ single crystal was introduced by Chen's group [94], which displayed the highest sensitivity of 23.6 $\mu C/mGy_{air}cm^2$, indicating high potential for practical applications.

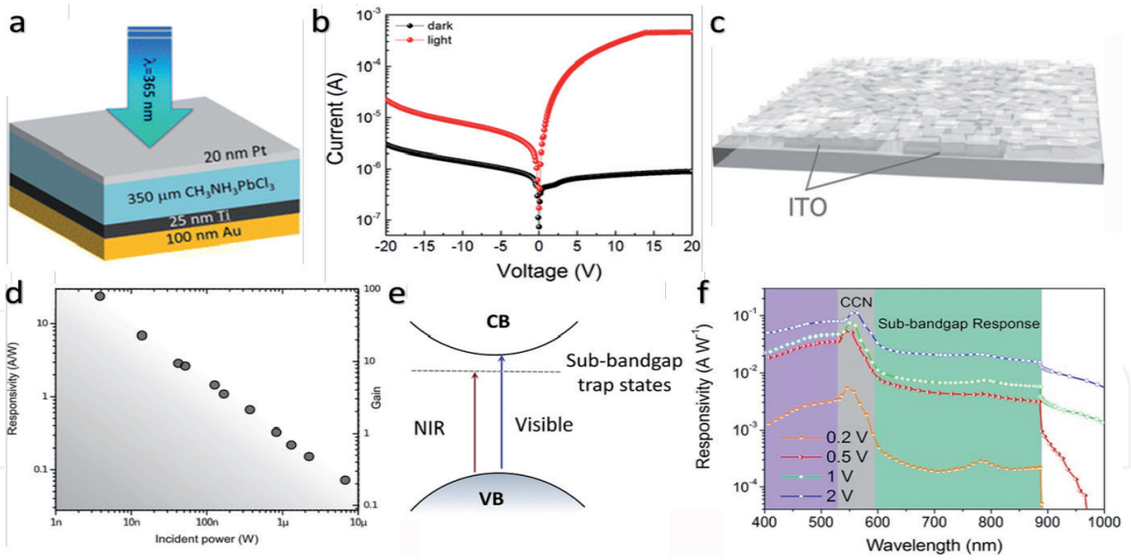

Figure 8.
8a, *device architecture of $MAPbCl_3$ crystal photodetector.* ***8b,*** I-V *curves of the photodetector under UV light (λ = 365 nm) and in the dark.* J. Phys. Chem. Lett. *[60], Copyright 2015.* ***8c,*** *schematic of planar-integrated $MAPbCl_3$ UV-detectors.* ***8d,*** R *and* G *values vs. incident light power.* Adv. Mater. *[83], Copyright 2016.* ***8e,*** *sub-gap electron trap state absorptions.* ***8f,*** R *values of $MAPbI_3$ photo-resistors under the illumination above the gap (visible, 600 nm) and below the gap (NIR, 900 nm).* Laser Photonics Rev. *[84], copyright 2016.*

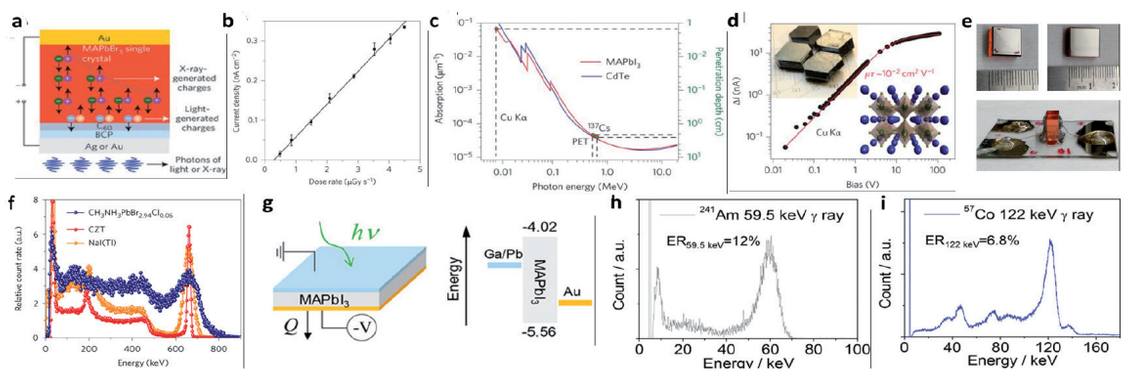

Figure 9.
9a, *structure of $MAPbBr_3$ crystal X-ray detector.* ***9b,*** *X-ray-generated photocurrent at various dose rates.* Nature Photonics *[53], copyright 2016.* ***9c,*** *attenuation coefficient and penetration depth of $MAPbI_3$ and CdTe.* ***9d,*** *photocurrent and a fit with Hecht model generated by Cu* Kα *X-ray radiation (8 keV) in a $MAPbI_3$ crystal.* Nature Photonics *[91], copyright 2016.* ***9e,*** *pictures of guard ring electrode side, anode side and side view of a $MAPbBr_{2.94}Cl_{0.06}$ crystal detector.* ***9f,*** *^{137}Cs energy spectrum obtained by crystal, CZT and NaI (Tl) detectors.* Nature Mater. *[92], Copyright 2017.* ***9 g,*** *schematic of a Schottky-type $MAPbI_3$ detector with asymmetrical electrode and the energy level diagram. Energy-resolved spectrum by Schottky-type $MAPbI_3$ detector (**9 h**) under ^{241}Am 59.5 keV γ-ray under −50 V and (**9i**) under ^{57}Co 122 keV γ-ray under −70 V.* ACS Photonics *[93], copyright 2018.*

4.2.5 In gamma-ray (γ-ray) region

Similar to X-ray detectors, the γ-ray detectors are also widely used in many fields, owing to the non-invasive detections. However, γ-ray detectors need to work in a weak radiation field pulse mode and perform event-by-event detections to sort out the intensity vs. the energy of the radiation quanta. Large and balanced μ and τ are needed for high-energy detection. Huang et al. reported high-quality $MAPbI_3$ crystals that were applied to γ-ray detection with a 4% efficiency when operating in the γ-voltaic mode [63]. Kovalenko et al. demonstrated $MAPbI_3$ crystals for γ-ray detection (**Figure 9c**), and a 59.6 keV ^{241}Am energy spectrum was acquired [91]. A fit of bias dependence of photocurrent with Hecht model indicated a high $\mu\tau$ product of $\sim 10^{-2}$ cm^2/V (**Figure 9d**) [95, 96].

Huang's group further reported a Cl^- dopant compensation of $MAPbBr_3$ single crystal process to fabricate a low-cost γ-ray detector [92]. $MAPbBr_{2.94}Cl_{0.06}$ crystals with a larger $\mu\tau$ product were equipped with a guard ring electrode to mitigate their leakage current (**Figure 9e**). The ^{137}Cs energy spectrum obtained by such crystals with a full-energy peak resolution of 6.50% is compared with the spectrum obtained by CZT and NaI(Tl) detectors (**Figure 9f**). A high-performance $MAPbI_3$ crystal γ-ray spectrometer was designed by Kanatzidis et al. [93], and the asymmetrical electrodes (Schottky-type) were applied to prohibit the hole injection from the anode or to reduce the leakage current (**Figure 9g**). The best energy resolution of the device for ^{241}Am 59.5 keV γ-rays was ~12%; while the best energy resolution achieved for ^{57}Co 122 keV was 6.8% (**Figure 9h** and **i**).

4.3 Light-emitting diodes (LEDs) and lasers

With the exceptional PL efficiency and high color purity, perovskite crystals can also perform as high-performance LEDs [97]. Most of the existing perovskite LEDs employ a polycrystalline film with sizes of nanometers to micrometers, and coherent light emission is a challenge [98]. In Yu's work, the LEDs with the structure of ITO/$MAPbBr_3$ micro-platelet/Au cathode had the turn-on voltage of about 1.8 V and could last for at least 54 h with a luminance of ~5000 cd/m^2 (**Figure 10a**) [99].

The excellent properties, including a small trap density, long lifetime and electron–hole diffusion length, and large carrier mobility, also make perovskite crystals suitable for laser devices with low lasing thresholds and high qualities. Xiong's group grew typical $MAPbI_3$ triangular nano-platelets and optically pumped them by a femtosecond-pulsed laser (**Figure 10b**) [100], and the peaks centered at λ = 776.7, 779.2, 781.9, 784.3, and 786.8 nm appeared over the spontaneous emission band with a FWHM of ~1.2 nm (**Figure 10c**), when the pump fluence was increased to 40.6 μJ/cm^2. Zhu et al. demonstrated room-temperature lasing via using $MAPbI_3$ crystal nanowire, which had a broad tenability covering the NIR to visible region [101].

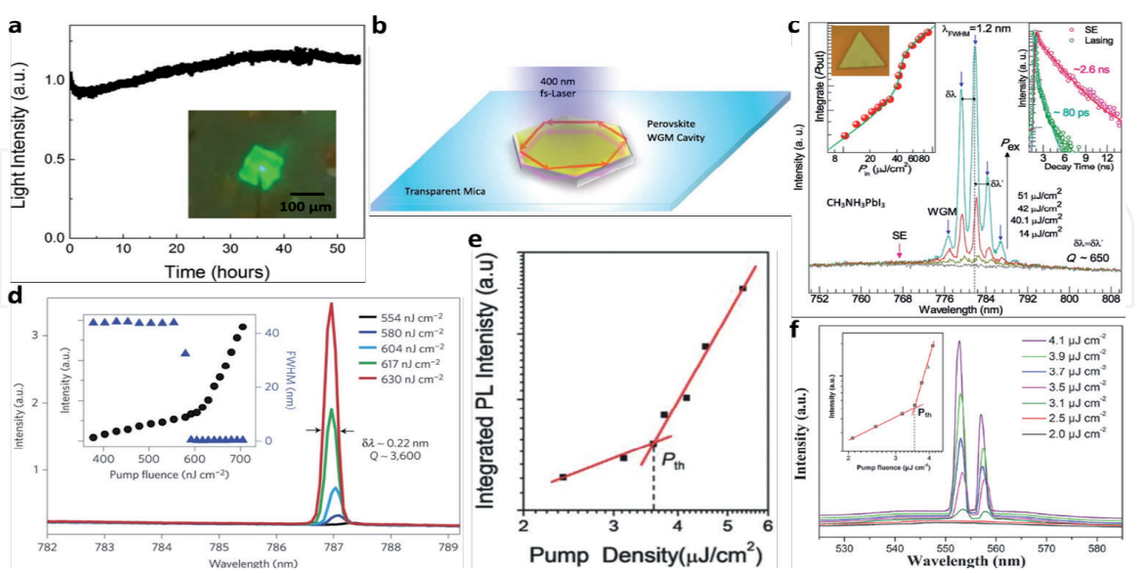

Figure 10.
***10a**, light emission intensity vs. time of a perovskite LED at −193°C. inset: A microscopic image at t = 12 h.* ACS Nano *[99], copyright 2018. **10b,** schematic for optical setup of a $CH_3NH_3PbI_3$ nanoplatelet. **10c,** evolution from spontaneous emission to lasing in a typical $CH_3NH_3PbI_3$ nanoplatelet. Inset left: Optical image of a nanoplate and plot of integrated P_{out}. Inset right: PL decay curve below (pink) and above (dark green) the threshold.* Nano Lett. *[100], Copyright 2014. **10d,** nanowire emission spectra. Inset: Integrated emission intensity and FWHM vs.* P. Nature Mater. *[101], Copyright 2015. **10e,** integrated PL intensity as a function of excitation density.* Adv. Mater. *[102], Copyright 2015. **10f,** emission spectra of perovskite microplates excited by different pump densities. Inset: Integrated PL intensity vs. pump density.* Adv. Mater. *[103], Copyright 2016.*

From **Figure 10d**, a sharp peak appeared at 787 nm in the representative emission spectra and grew rapidly with increasing the pump laser fluence (P) with the lasing threshold P_{Th} of ~595 nJ/cm^2. Additionally, $MAPbBr_3$ crystal square micro-disks were synthesized into a 557-nm single-mode laser based on a built-in whispering gallery mode micro-resonator by Fu's group [102], from which a P_{Th} = 3.6 μJ/cm^2 was observed, and a sublinear regime was observed below the threshold (**Figure 10e**). Uniform-sized $MAPbBr_3$ microplates were also created by Jiang et al. by using "liquid knife" and were made into lasers [103]. A 400-nm pulsed laser beam was used as a pump source to excite microplates, and a spontaneous emission peak centered at 550 nm with a FWHM of 20 nm was observed (**Figure 10f**).

5. Challenges and open issues

Hybrid perovskite single crystals have shown great potential in high-performance optoelectronic devices; however, several challenges and issues still remain in terms of their practical applications. They mainly include (1) the effects of surface defects, (2) the large-area fabrication, as well as (3) the stability of the perovskite single crystal devices and (4) the health and environmental concerns.

5.1 Surface defects

The absence of grain boundaries makes perovskite crystals acquire better optical and charge transport properties than their polycrystalline counterparts. However, the surface of crystals usually possesses lots of chemical impurities, dangling bonds, surface dislocations, and under-coordinated atoms, and becomes disordered owing to hydration, thus decreasing the carrier mobility and carrier diffusion length and promote the recombination of carriers near the crystal surface [76, 104–106]. Thus, the further decrease of defects, especially the surface defects, is required, aiming to gain high-quality perovskite crystals. To realize high-performance optoelectronic devices based on perovskite crystals with low-level surface defects, more research should be carried out on the surface passivation.

5.2 Large-area fabrication

Hybrid perovskite thin crystals are freer of grain boundaries and exhibit better transport properties than those of the polycrystalline candidates, so their large-area fabrication will ensure a promising future. However, the embedding of volatile and vulnerable organic components on fragile inorganic framework makes them difficult to be fabricated with a large area by deposition techniques or solution-based methods [42, 54]. Furthermore, thin crystals were grown directly on conductive substrates like FTO- or ITO-glass [42, 56], and tailored substrates, such as SiO_2/Si [97], which provide in-situ growth for thin crystals and be directly made into devices. Nevertheless, these large-area thin crystals have rough surfaces and a great number of surface defects, and thus their optoelectronic properties remain inferior to the bulk counterparts. Further optimization of growth methods for large-area thin crystals is needed for industry productions in future.

5.3 Long-term stability

Low stability of the current hybrid perovskite crystal devices hinders their broad practical application. Several factors that affect the device stability, like ion migration [107, 108], can cause hysteresis and photo-induced phase separation, and the interaction

between single crystals and their surroundings lies in the degradation of perovskite by humidity and light [109–111]. Therefore, to further enhance the stability of single crystal devices, optimized device structures should be designed to control the ion migrations. Meanwhile, various compositions and interface engineering approaches are also intensively investigated to confront this critical issue. In addition, encapsulation has been demonstrated to be a valid method to protect hybrid perovskite devices.

5.4 Health and environmental concerns

The growth of hybrid perovskite crystals adopt heavy metal ions, like lead (Pb) or tin (Sn), and organic functional groups, which can impact both the environment and human health. This critical issue needs to be overcome, aiming for further commercialization. As for the common $MAPbI_3$ perovskite crystal, the Pb-ion is toxic to both the human health and natural environment; while the organic solvents used during the growth process of crystals are also toxic and easily penetrate into the human body [112]. To solve these problems, capsulation and recycling are needed in the use of crystal materials and organic solvents. Furthermore, other alternative metals to Pb, with a lower toxicity, are also being studied, such as bismuth and antimony [113, 114], and thus, the optoelectronic properties of these Pb-free perovskite crystals need to be explored further for device applications.

6. Conclusions

More recently, hybrid perovskite crystals, having different dimensional forms: bulk and thin crystals, and micro−/nano-plates, have been widely explored as functional layers for optoelectronic devices owing to their excellent physical properties combined with the advantage of ease of processing. Although these types of devices are still in the early stages of development, a strong potential for a variety of technological and commercial applications clearly remains. Here, we presented a comprehensive overview of the recent advances in hybrid perovskite crystals with respect to the background knowledge on the optoelectronic properties and charge transport dynamics of crystals, and their applications in the area of optoelectronic devices, and a fundamental understanding of the device performance. We summarized the main growth methods for the bulk crystals and also some modified and optimized approaches to synthesize thin crystals. The detailed discussions are focused on charge transport characteristics, operation mechanisms, and challenges, aiming to provide a critical understanding of further advance in materials design and device engineering in a variety of optoelectronic technologies.

In conclusion, the research progress achieved to date in the area of perovskite crystal optoelectronic devices, with the emphasis placed on challenges faced by the research community, has been summarized systematically, and finally perspective on the opportunities offered by this emerging family to photoactive materials in practical and commercial technologies is also proposed. Further exploration of high-quality perovskite crystals, combined with an in-depth understandings of working mechanism of devices, indicates a promising future for wide applications with markedly-enhanced performance.

Acknowledgements

The author acknowledges support from Discovery Early Career Researcher Award (DECRA) (DE180100167) from the Australian Research Council (ARC).

Conflict of interest

There are no conflicts to declare.

Author details

Feng Li
School of Physics, Faculty of Science, The University of Sydney, Sydney, NSW, Australia

*Address all correspondence to: feng.li2@sydney.edu.au

References

[1] Mitzi, D. B. Templating and structural engineering in organic–inorganic perovskites. *J. Chem. Soc., Dalton Trans.*, 2001, 1-12.

[2] Green, M. A.; Ho-Baillie, A.; Snaith, H. J. The emergence of perovskite solar cells. *Nature photonics* 2014, 8, 506.

[3] Zhang, D.; Zhu, Y.; et al. Atomic-resolution transmission electron microscopy of electron beam–sensitive crystalline materials. *Science* 2018, 359, 675-679.

[4] Ke, W.; Mao, L.; et al. Compositional and solvent engineering in Dion–Jacobson 2D perovskites boosts solar cell efficiency and stability. *Adv. Energy Mater.* 2019, 9, 1803384.

[5] Li, S.; Tong, S.; et al. Fast-response and high-responsivity $FA_xMA_{(1-x)}PbI_3$ photodetectors fabricated via doctor-blading deposition in ambient condition. *Org. Electron.* 2018, 52, 190-194.

[6] Wang, H.; Wu, H.; et al. Controllable $Cs_xFA_{1-x}PbI_3$ single-crystal morphology via rationally regulating the diffusion and collision of micelles toward high-performance photon detectors. *ACS Appl. Mater. Interfaces* 2019, 11, 13812-13821.

[7] Hou, X.; Xu, M.; et al. High performance printable perovskite solar cells based on $Cs_{0.1}FA_{0.9}PbI_3$ in mesoporous scaffolds. *J. Power Sources* 2019, 415, 105-111.

[8] Wang, M.; Jiang, X.; et al. High-performance and stable mesoporous perovskite solar cells via well-crystallized $FA_{0.85}MA_{0.15}Pb(I_{0.8}Br_{0.2})_3$. *ACS Appl. Mater. Interfaces* 2018, 11, 2989-2996.

[9] Babayigit, A.; Thanh, D. D.; et al. Assessing the toxicity of Pb- and Sn-based perovskite solar cells in model organism *Danio rerio. Sci. Rep.* 2016, 6, 1-11.

[10] Ma, H.; Ma, Y.; et al. Experimental phonon dispersion and lifetimes of tetragonal $CH_3NH_3PbI_3$ perovskite crystals. *J. Phys. Chem. Let.* 2018, 10, 1-6.

[11] Ju, D.; Zheng, X.; et al. Reversible band gap narrowing of Sn-based hybrid perovskite single crystal with excellent phase stability. *Angew. Chem. Int. Ed.* 2018, 57, 14868-14872.

[12] Ju, D.; Dang, Y.; et al. Tunable band gap and long carrier recombination lifetime of stable mixed $CH_3NH_3Pb_xSn_{1-x}Br_3$ single crystals. *Chem. Mater.* 2018, 30, 1556-1565.

[13] Shao, S.; Liu, J.; et al. Highly reproducible Sn-based hybrid perovskite solar cells with 9% efficiency. *Adv. Energy Mater.* 2018, 8, 1702019.

[14] Li, C.; Lu, X.; et al. Formability of ABX_3 (X= F, Cl, Br, I) halide perovskites. *Acta Crystallogr. B Struct. Sci.* 2008, 64, 702-707.

[15] Shi, D.; Adinolfi, V.; et al. Low trap-state density and long carrier diffusion in organolead trihalide perovskite single crystals. *Science* 2015, 347, 519-522.

[16] Kojima, A.; Teshima, K.; et al. Organometal halide perovskites as visible-light sensitizers for photovoltaic cells. *J. Am. Chem. Soc.* 2009, 131, 6050-6051.

[17] Xiao, Z.; Bi, C.; et al. Efficient, high yield perovskite photovoltaic devices grown by interdiffusion of solution-processed precursor stacking layers. *Energy Environ. Sci.* 2014, 7, 2619-2623.

[18] Liu, M.; Johnston, M. B.; Snaith, H. J. Efficient planar heterojunction perovskite solar cells by vapour deposition. *Nature* 2013, 501, 395-398.

[19] Xiao, M.; Huang, F.; et al. A fast deposition-crystallization procedure for highly efficient lead iodide perovskite thin-film solar cells. *Angew. Chem. Int. Ed.* 2014, 53, 9898-9903.

[20] Zhu, W.; Bao, C.; et al. An efficient planar-heterojunction solar cell based on wide-bandgap $CH_3NH_3PbI_{2.1}Br_{0.9}$ perovskite film for tandem cell application. *Chem. Commun.* 2016, 52, 304-307.

[21] Heo, J. H.; Im, S. H.; et al. Efficient inorganic–organic hybrid heterojunction solar cells containing perovskite compound and polymeric hole conductors. *Nature photonics* 2013, 7, 486.

[22] Jeon, N. J.; Noh, J. H.; et al. Solvent engineering for high-performance inorganic–organic hybrid perovskite solar cells. *Nature Mater.* 2014, 13, 897-903.

[23] Lee, M. M.; Teuscher, J.; et al. Efficient hybrid solar cells based on meso-super structured organometal halide perovskites. *Science* 2012, 338, 643-647.

[24] Filip, M. R.; Eperon, G. E.; et al. Steric engineering of metal-halide perovskites with tunable optical band gaps. *Nature Commun.* 2014, 5, 1-9.

[25] D'Innocenzo, V.; Srimath Kandada, A. R.; et al. Tuning the light emission properties by band gap engineering in hybrid lead halide perovskite. *J. Am. Chem. Soc.* 2014, 136, 17730-17733.

[26] Sum, T. C.; Mathews, N. Advancements in perovskite solar cells: photophysics behind the photovoltaics. *Energy Environ. Sci.* 2014, 7, 2518-2534.

[27] Choi, H.; Jeong, J.; et al. Cesium-doped methylammonium lead iodide perovskite light absorber for hybrid solar cells. *Nano Energy* 2014, 7, 80-85.

[28] Kim, Y. H.; Cho, H.; et al. Multicolored organic/inorganic hybrid perovskite light-emitting diodes. *Adv. Mater.* 2015, 27, 1248-1254.

[29] NREL. Efficiency chart. https://www.nrel.gov/pv/assets/pdfs/pv-efficiency-chart.20181214.pdf.

[30] Hu, X.; Zhang, X.; et al. High-performance flexible broadband photodetector based on organolead halide perovskite. *Adv. Funct. Mater.* 2014, 24, 7373-7380.

[31] Chin, X. Y.; Cortecchia, D.; et al. Lead iodide perovskite light-emitting field-effect transistor. *Nature Commun.* 2015, 6, 7383.

[32] Li, F.; Ma, C.; et al. Ambipolar solution-processed hybrid perovskite phototransistors. *Nature Commun.* 2015, 6, 8238.

[33] Meng, L.; Yao, E. P.; et al. Pure formamidinium-based perovskite light-emitting diodes with high efficiency and low driving voltage. *Adv. Mater.* 2017, 29, 1603826.

[34] Liu, P.; He, X.; et al. Organic–inorganic hybrid perovskite nanowire laser arrays. *ACS Nano* 2017, 11, 5766-5773.

[35] Duan, H.-S.; Zhou, H.; et al. The identification and characterization of defect states in hybrid organic–inorganic perovskite photovoltaics. *Phys. Chem. Chem. Phys.* 2015, 17, 112-116.

[36] Zheng, X.; Chen, B.; et al. Defect passivation in hybrid perovskite solar cells using quaternary ammonium halide anions and cations. *Nature Energy* 2017, 2, 1-9.

[37] Liu, Z.; Hu, J.; et al. Chemical reduction of intrinsic defects in thicker heterojunction planar perovskite solar cells. *Adv. Mater.* 2017, 29, 1606774.

[38] Fang, H.-H.; Adjokatse, S.; et al. Ultrahigh sensitivity of methylammonium lead tribromide perovskite single crystals to environmental gases. *Sci. Adv.* 2016, 2, e1600534.

[39] Huang, J.; Shao, Y.; Dong, Q. Organometal trihalide perovskite single crystals: a next wave of materials for 25% efficiency photovoltaics and applications beyond? *J. Phys. Chem. Lett.* 2015, 6, 3218-3227.

[40] Zhang, F.; Yang, B.; et al. Extra-long electron–hole diffusion lengths in $CH_3NH_3PbI_{3-x}Cl_x$ perovskite single crystals. *J. Mater. Chem. C* 2017, 5, 8431-8435.

[41] Chen, B.-X.; Li, W.-G.; et al. Large-grained perovskite films via $FA_xMA_{1-x}Pb(I_xBr_{1-x})_3$ single crystal precursor for efficient solar cells. *Nano Energy* 2017, 34, 264-270.

[42] Saidaminov, M. I.; Adinolfi, V.; et al. Planar-integrated single-crystalline perovskite photodetectors. *Nature Commun.* 2015, 6, 1-7.

[43] Li, S.; Zhang, C.; et al. Metal halide perovskite single crystals: from growth process to application. *Crystals* 2018, 8, 220.

[44] Liu, Y.; Yang, Z.; Liu, S. Recent progress in single-crystalline perovskite research Including crystal preparation, property evaluation, and applications. *Adv. Sci.* 2018, 5, 1700471.

[45] Chen, Y.; He, M.; et al. Structure and growth control of organic–inorganic halide perovskites for optoelectronics: from polycrystalline films to single crystals. *Adv. Sci.* 2016, 3, 1500392.

[46] Ding, J.; Yan, Q. Progress in organic-inorganic hybrid halide perovskite single crystal: growth techniques and applications. *Sci. China Mater.* 2017, 60, 1063-1078.

[47] Dang, Y.; Liu, Y.; et al. Bulk crystal growth of hybrid perovskite material $CH_3NH_3PbI_3$. *CrystEngComm* 2015, 17, 665-670.

[48] Su, J.; Chen, D.; Lin, C. Growth of large $CH_3NH_3PbX_3$ (X= I, Br) single crystals in solution. *J. Cryst. Growth* 2015, 422, 75-79.

[49] Fang, Y.; Dong, Q.; et al. Highly narrowband perovskite single-crystal photodetectors enabled by surface-charge recombination. *Nature Photonics* 2015, 9, 679.

[50] Saidaminov, M. I.; Abdelhady, A. L.; et al. High-quality bulk hybrid perovskite single crystals within minutes by inverse temperature crystallization. *Nature Commun.* 2015, 6, 1-6.

[51] Zhang, Y.; Liu, Y.; et al. Perovskite $CH_3NH_3Pb(Br_xI_{1-x})_3$ single crystals with controlled composition for fine-tuned bandgap towards optimized optoelectronic applications. *J. Mater. Chem. C* 2016, 4, 9172-9178.

[52] Zhang, B.; Yan, J.; et al. Effect of the modulating of organic content on optical properties of single-crystal perovskite. *Opt. Mater.* 2016, 62, 273-278.

[53] Wei, H.; Fang, Y.; et al. Sensitive X-ray detectors made of methylammonium lead tribromide perovskite single crystals. *Nature Photonics* 2016, 10, 333.

[54] Peng, W.; Wang, L.; et al. Solution-grown monocrystalline hybrid perovskite films for hole-transporter-free solar cells. *Adv. Mater.* 2016, 28, 3383-3390.

[55] Liu, Y.; Zhang, Y.; et al. Thinness- and shape-controlled growth for

ultrathin single-crystalline perovskite wafers for mass production of superior photoelectronic devices. *Adv. Mater.* 2016, 28, 9204-9209.

[56] Rao, H. S.; Li, W. G.; et al. In-situ growth of 120-cm^2 $CH_3NH_3PbBr_3$ perovskite crystal film on FTO glass for narrowband-photodetectors. *Adv. Mater.* 2017, 29, 1602639.

[57] Chen, Y.-X.; Ge, Q.-Q.; et al. General space-confined on-substrate fabrication of thickness-adjustable hybrid perovskite single-crystalline thin films. *J. Am. Chem. Soc.* 2016, 138, 16196-16199.

[58] Lee, L.; Baek, J.; et al. Wafer-scale single-crystal perovskite patterned thin films based on geometrically-confined lateral crystal growth. *Nature Commun.* 2017, 8, 1-8.

[59] Gu, Z.; Huang, Z.; et al. A general printing approach for scalable growth of perovskite single-crystal films. *Sci. Adv.* 2018, 4, eaat2390.

[60] Maculan, G.; Sheikh, A. D.; et al. $CH_3NH_3PbCl_3$ single crystals: inverse temperature crystallization and visible-blind UV-photodetector. *J. Phys. Chem. Lett.* 2015, 6, 3781-3786.

[61] Wenger, B.; Nayak, P. K.; et al. Consolidation of the optoelectronic properties of $CH_3NH_3PbBr_3$ perovskite single crystals. *Nature Commun.* 2017, 8, 1-10.

[62] Zhang, Y.; Liu, Y.; et al. High-quality perovskite $MAPbI_3$ single crystals for broad-spectrum and rapid response integrate photodetector. *J. Energy Chem.* 2018, 27, 722-727.

[63] Dong, Q.; Fang, Y.; et al. Electron-hole diffusion lengths >175 μm in solution-grown $CH_3NH_3PbI_3$ single crystals. *Science* 2015, 347, 967-970.

[64] Yi, H. T.; Wu, X.; et al. Intrinsic charge transport across phase transitions in hybrid organo-inorganic perovskites. *Adv. Mater.* 2016, 28, 6509-6514.

[65] Valverde-Chávez, D. A.; Ponseca, C. S.; et al. Intrinsic femtosecond charge generation dynamics in single crystal $CH_3NH_3PbI_3$. *Energy Environ. Sci.* 2015, 8, 3700-3707.

[66] Yu, W.; Li, F.; et al. Single crystal hybrid perovskite field-effect transistors. *Nature Commun.* 2018, 9, 1-10.

[67] Edri, E.; Kirmayer, S.; et al. High open-circuit voltage solar cells based on organic–inorganic lead bromide perovskite. *J. Phys. Chem. Lett.* 2013, 4, 897-902.

[68] Giorgi, G.; Yamashita, K. Organic–inorganic halide perovskites: an ambipolar class of materials with enhanced photovoltaic performances. *J. Mater. Chem. A* 2015, 3, 8981-8991.

[69] Ball, J. M.; Petrozza, A., Defects in perovskite-halides and their effects in solar cells. *Nature Energy* 2016, 1, 1-13.

[70] Zhang, M.; Yu, H.; et al. Composition-dependent photoluminescence intensity and prolonged recombination lifetime of perovskite $CH_3NH_3PbBr_{3-x}Cl_x$ films. *Chem. Commun.* 2014, 50, 11727-11730.

[71] Fang, Y.; Wei, H.; et al. Quantification of re-absorption and re-emission processes to determine photon recycling efficiency in perovskite single crystals. *Nature Commun.* 2017, 8, 14417.

[72] Chen, Z.; Dong, Q.; et al. Thin single crystal perovskite solar cells to harvest below-bandgap light absorption. *Nature Commun.* 2017, 8, 1-7.

[73] Dong, Q.; Song, J.; et al. Lateral-structure single-crystal hybrid perovskite solar cells via piezoelectric poling. *Adv. Mater.* 2016, 28, 2816-2821.

[74] Chen, Z.; Turedi, B.; et al. Single-crystal $MAPbI_3$ perovskite solar cells exceeding 21% power conversion efficiency. *ACS Energy Lett.* 2019, 4, 1258-1259.

[75] Bao, C.; Chen, Z.; et al. Low-noise and large-linear-dynamic-range photodetectors based on hybrid-perovskite thin-single-crystals. *Adv. Mater.* 2017, 29, 1703209.

[76] Lian, Z.; Yan, Q.; et al. High-performance planar-type photodetector on (100) facet of $MAPbI_3$ single crystal. *Sci. Rep.* 2015, 5, 16563.

[77] Cao, M.; Tian, J.; et al. Perovskite heterojunction based on $CH_3NH_3PbBr_3$ single crystal for high-sensitive self-powered photodetector. *Appl. Phys. Lett.* 2016, 109, 233303.

[78] Qin, X.; Yao, Y.; et al. Perovskite photodetectors based on $CH_3NH_3PbI_3$ single crystals. *Chem. Asian J.* 2016, 11, 2675-2679.

[79] Yang, Z.; Deng, Y.; et al. High-performance single-crystalline perovskite thin-film photodetector. *Adv. Mater.* 2018, 30, 1704333.

[80] Cheong, P.; Chang, K.-F.; et al. A ZigBee-based wireless sensor network node for ultraviolet detection of flame. *IEEE Trans. Ind. Electron.* 2011, 58, 5271-5277.

[81] Li, M.; Li, W.; et al. On-site determination and monitoring of real-time fluence delivery for an operating UV reactor based on a true fluence rate detector. *Environ. Sci. Technol.* 2017, 51, 8094-8100.

[82] Ojeda, C. B.; Rojas, F. S. Process analytical chemistry: applications of ultraviolet/visible spectrometry in environmental analysis: an overview. *Appl. Spectrosc. Rev.* 2009, 44, 245-265.

[83] Adinolfi, V.; Ouellette, O.; et al. Fast and sensitive solution-processed visible-blind perovskite UV photodetectors. *Adv. Mater.* 2016, 28, 7264-7268.

[84] Lin, Q.; Armin, A.; et al. Near infrared photodetectors based on sub-gap absorption in organohalide perovskite single crystals. *Laser Photonics Rev.* 2016, 10, 1047-1053.

[85] Dong, R.; Fang, Y.; et al. High-gain and low-driving-voltage photodetectors based on organolead triiodide perovskites. *Adv. Mater.* 2015, 27, 1912-1918.

[86] Chin, A.; Vaddiraju, S.; et al. Near-infrared semiconductor subwavelength-wire lasers. *Appl. Phys. Lett.* 2006, 88, 163115.

[87] Cheng, S.-Q.; Cai, B.; Zhu, Y.-M. Black silicon as absorber for near-infrared photo-thermal conversion, 2015 Opto-Electronics and Communications Conference (OECC), IEEE: 2015; pp 1-3.

[88] Du, K.-K.; Li, Q.; et al. Control over emissivity of zero-static-power thermal emitters based on phase-changing material GST. *Light Sci. Appl.* 2017, 6, e16194-e16194.

[89] Wang, Z.; Li, Y.; et al. Pure near-infrared to near-infrared up-conversion of multifunctional Tm^{3+} and Yb^{3+} co-doped NaGd $(WO_4)_2$ nanoparticles. *J. Mater. Chem. C* 2014, 2, 4495-4501.

[90] Naczynski, D.; Tan, M.; et al Rare-earth-doped biological composites as in vivo shortwave infrared reporters. *Nature Commun.* 2013, 4, 1-10.

[91] Yakunin, S.; Dirin, D. N.; et al. Detection of gamma photons using solution-grown single crystals of hybrid lead halide perovskites. *Nature Photonics* 2016, 10, 585.

[92] Wei, H.; DeSantis, D.; et al. Dopant compensation in alloyed

$CH_3NH_3PbBr_{3-x}Cl_x$ perovskite single crystals for gamma-ray spectroscopy. *Nature Mater.* 2017, 16, 826-833.

[93] He, Y.; Ke, W.; et al. Resolving the energy of γ-ray photons with $MAPbI_3$ single crystals. *ACS Photonics* 2018, 5, 4132-4138.

[94] Wang, X.; Zhao, D.; et al. PIN diodes array made of perovskite single crystal for X-ray imaging. *Phys. Status Solidi RRL* 2018, 12, 1800380.

[95] Street, R.; Ready, S.; et al. Comparison of PbI_2 and HgI_2 for direct detection active matrix X-ray image sensors. *J. Appl. Phys.* 2002, 91, 3345-3355.

[96] Kabir, M. Z.; Kasap, S. Charge collection and absorption-limited sensitivity of X-ray photoconductors: Applications to *a*-Se and HgI_2. *Appl. Phys. Lett.* 2002, 80, 1664-1666.

[97] Nguyen, V.-C.; Katsuki, H.; et al. Single-crystal perovskite $CH_3NH_3PbBr_3$ prepared by cast capping method for light-emitting diodes. *Jpn. J. Appl. Phys.* 2018, 57, 04FL10.

[98] Chih, Y. K.; Wang, J. C.; et al. NiO_x electrode interlayer and CH_3NH_2/$CH_3NH_3PbBr_3$ Interface treatment to markedly advance hybrid perovskite-based light-emitting diodes. *Adv. Mater.* 2016, 28, 8687-8694.

[99] Chen, M.; Shan, X.; et al. Manipulating ion migration for highly stable light-emitting diodes with single-crystalline organometal halide perovskite microplatelets. *ACS Nano* 2017, 11, 6312-6318.

[100] Zhang, Q.; Ha, S. T.; et al. Room-temperature near-infrared high-Q perovskite whispering-gallery planar nanolasers. *Nano Lett.* 2014, 14, 5995-6001.

[101] Zhu, H.; Fu, Y.; et al. Lead halide perovskite nanowire lasers with low lasing thresholds and high quality factors. *Nature Mater.* 2015, 14, 636-642.

[102] Liao, Q.; Hu, K.; et al. Perovskite microdisk microlasers self-assembled from solution. *Adv. Mater.* 2015, 27, 3405-3410.

[103] Feng, J.; Yan, X.; et al. "Liquid knife" to fabricate patterning single-crystalline perovskite microplates toward high-performance laser arrays. *Adv. Mater.* 2016, 28, 3732-3741.

[104] Wu, B.; Nguyen, H. T.; et al. Discerning the surface and bulk recombination kinetics of organic–inorganic halide perovskite single crystals. *Adv. Energy Mater.* 2016, 6, 1600551.

[105] Murali, B.; Yengel, E.; et al. The surface of hybrid perovskite crystals: a boon or bane. *ACS Energy Lett.* 2017, 2, 846-856.

[106] Yang, Y.; Yang, M.; et al. Top and bottom surfaces limit carrier lifetime in lead iodide perovskite films. *Nature Energy* 2017, 2, 1-7.

[107] Yuan, Y.; Huang, J. Ion migration in organometal trihalide perovskite and its impact on photovoltaic efficiency and stability. *Acc. Chem. Res.* 2016, 49, 286-293.

[108] Deng, Y.; Xiao, Z.; Huang, J. Light-induced self-poling effect on organometal trihalide perovskite solar cells for increased device efficiency and stability. *Adv. Energy Mater.* 2015, 5, 1500721.

[109] Li, W.; Fan, J.; et al. Aquointermediate assisted highly orientated perovskite thin films toward thermally stable and efficient solar cells. *Adv. Energy Mater.* 2017, 7, 1601433.

[110] Grancini, G.; D'Innocenzo, V.; et al. $CH_3NH_3PbI_3$ perovskite single crystals: surface photophysics and their

interaction with the environment. *Chem. Sci.* 2015, 6, 7305-7310.

[111] Ecker, B. R.; Wang, C.; et al. Intrinsic behavior of $CH_3NH_3PbBr_3$ single crystals under light illumination. *Adv. Mater. Interfaces* 2018, 5, 1801206.

[112] Williams, A. C.; Barry, B. W. Penetration enhancers. *Adv. Drug Deliv. Rev.* 2012, 64, 128-137.

[113] Lyu, M.; Yun, J.-H.; et al. Organic–inorganic bismuth (III)-based material: A lead-free, air-stable and solution-processable light-absorber beyond organolead perovskites. *Nano Res.* 2016, 9, 692-702.

[114] Leng, M.; Chen, Z.; et al. Lead-free, blue emitting bismuth halide perovskite quantum dots. *Angew. Chem. Int. Ed.* 2016, 55, 15012-15016.